crystals

MDPI

Article

Toughening Mechanism of $CaAl_{12}O_{19}$ in Red Mud–Al_2O_3 Composite Ceramics

Shiwei Jiang [1], Anmin Li [2,*] and Zhengliang Wang [2]

[1] School of Resources, Environment and Materials, Guangxi University, Nanning 530004, China; 2215391037@st.gxu.edu.cn
[2] State Key Laboratory of Featured Metal Materials and Life-Cycle Safety for Composite Structures, Guangxi University, Nanning 530004, China; 2315391099@st.gxu.edu.cn
* Correspondence: lianmin@gxu.edu.cn

Abstract: The utilization of red mud in the production of ceramic products represents an efficient approach for harnessing red mud resources. Composite ceramics were prepared from Al_2O_3, red mud, and Cr_2O_3 by atmospheric pressure sintering, and the phase composition and microscopic morphology of the composite ceramics were investigated by XRD, SEM, and EDS. The flexural strength and fracture toughness of composite ceramics were measured by three-point bending and SENB methods. The results showed that the composite ceramics sintered at 1500 °C with the addition of 1.5 wt.% Cr_2O_3 had a flexural strength of 297.03 MPa, a hardness of 17.44 GPa, and a densification of 97.75% and fracture toughness of 6.57 MPa·$m^{1/2}$. The addition of Cr_2O_3 helps to improve the low strength of red mud composite ceramic samples. The $CaAl_{12}O_{19}$ phase can form a similar "endo-crystalline" structure with Al_2O_3 grains, which changes the fracture mode of the ceramics and thus significantly improves the fracture toughness. The wettability tests conducted on Cu and RM–Al_2O_3 composite ceramic materials revealed that the composites exhibited non-wetting behavior towards Cu at elevated temperatures, while no interfacial reactions or elemental diffusion were observed. Composites have higher surface energy than Al_2O_3 ceramic at high temperatures. The present study provides a crucial foundation for enhancing the comprehensive utilization value of red mud and the application of red mud ceramics in the field of electronic packaging.

Keywords: red mud; alumina composite ceramics; mechanical properties; surface energy

check for updates

Citation: Jiang, S.; Li, A.; Wang, Z. Toughening Mechanism of $CaAl_{12}O_{19}$ in Red Mud–Al_2O_3 Composite Ceramics. *Crystals* **2024**, *14*, 924. https://doi.org/10.3390/cryst14110924

Academic Editor: Ram S. Katiyar

Received: 28 September 2024
Revised: 16 October 2024
Accepted: 22 October 2024
Published: 26 October 2024

Copyright: © 2024 by the authors. Licensee MDPI, Basel, Switzerland. This article is an open access article distributed under the terms and conditions of the Creative Commons Attribution (CC BY) license (https://creativecommons.org/licenses/by/4.0/).

1. Introduction

"Red mud" (RM) refers to solid waste that is discharged during the process of generating Al_2O_3. Comprised primarily of various complex mineral phases, red mud possesses a highly alkaline nature. The current situation lacks an effective solution for red mud treatment, primarily relying on the construction of multiple containment dams to store the red mud [1,2]. With prolonged stockpiling, the harmful elements in red mud can contaminate nearby water sources and cause soil alkalization. At the same time, red mud is highly adsorbent, and dams may also be at risk of breaking during the rainy season. This seriously jeopardizes the safety of people's lives and property. Wang et al. [3] took red mud and kaolin as raw materials, changed the reaction path of mullite by adding $(NH_4)_6Mo_7O_{24}$, and sintered the sample at 1180 °C to obtain a sample with a flexion strength of 185.6 MPa, a bulk weight of 1.45 g/cm^3, and a water absorption rate of 5.5%. He et al. [4] used red mud, clay and raw materials, and a 20% RM ceramic body was prepared by sintering at 1050 °C for 2 h. The ceramic body had a bulk weight of 1.69 g/cm^3, loss on ignition of 10.32%, sintering shrinkage of 5.71%, water absorption of 19.91%, and compressive strength of 36.5 MPa. Pérez-Villarejo et al. [5] mixed red mud and clay in a 1:1 ratio and sintered at 950 °C for 1 h. The samples obtained had a linear shrinkage of 0.46%, a water absorption of 21.00%, a weight loss of 12.6% after sintering, and a compressive strength of 52.54 MPa. Triviño et al. [6] mixed red mud and granite waste in a ratio of 6:4 and sintered

the sample at 1150 °C, and the sample obtained had the highest hardness (545.6 kgf/mm^2) and a flexural strength of 27 MPa. The addition of red mud should be carefully controlled in order to enhance the properties of ceramic products, as red mud itself contains high levels of Na_2O and CaO, which are detrimental to the properties of cement and ceramics. Furthermore, the high content of red mud in the sample also makes it easier for the harmful elements in the red mud to leak into the environment, which limits the application of red mud ceramic products.

Cr_2O_3 is often used as one of the additives to improve the physical properties of alumina, Cr_2O_3 and Al_2O_3 have isostructural corundum crystal structures (hexagonal system with the same space group R-3c), and it is well known that Cr_2O_3 forms a substitutional solid solution in the Al_2O_3 lattice by ion exchange with Al^{3+} and does not form any eutectic in the whole compositional range [7]. Several studies have shown the addition of Cr_2O_3 to Al_2O_3 in different ratios to improve the mechanical properties of ceramics by means of different solidification techniques. Kafkaslıoğlu Yıldız et al. [8] investigated the effect of Cr_2O_3 additions with different volume ratios (0.5, 1, 5 vol.%) on the microstructure and mechanical properties of Al_2O_3. When the Cr_2O_3 addition was 0.5 vol.%, the flexural strength of the material was 286 MPa, which increased by 44% compared to pure Al_2O_3. This is due to the localized compressive stress caused by the grain boundary alteration of Cr^{3+} ions. The crack extension behavior changes from a predominantly along-crystal extension to mixed along-crystal and through-crystal extensions with the addition of localized compressive stresses from Cr_2O_3, leading to grain boundary strengthening. Azhar et al. [9] reported that the microstructures of ZTA composite were significantly affected by the addition of a small amount of Cr_2O_3 (∼0.6 wt.%), with the grains becoming larger and acquiring a plate-like shape. The fracture toughness was increased from 4.41 MPa·m$^{1/2}$ to 4.73 MPa·m$^{1/2}$. Manshor et al. [10] reported that with addition of 0.6 wt.% of Cr_2O_3 to the composite, an optimum density of 4.0630 g/cm^3, hardness of 1681 HV, and fracture toughness of 7.15 MPa·m$^{1/2}$ were obtained. The addition of 0.6 wt.% Cr_2O_3 led to the formation of large plate-like grains, enhancing the interaction between the crack and the matrix grains. The inter-granular fracture mode caused the cracks to spread along the borders of the grains, eventually increasing the strength due to grain deflection.

The work in this paper is motivated by the exhaust gas recirculation (EGR) system utilized in diesel engines, which introduces an appropriate quantity of exhaust gas into the cylinder to participate in combustion. As a result, it effectively reduces the maximum temperature within the cylinder and subsequently mitigates NOx emissions. Similarly, adding an appropriate amount of red mud to Al_2O_3 ceramics can be used as a sintering aid for the sintering of Al_2O_3 ceramics, so as to realize the resource utilization of red mud. In this paper, the effects of different sintering temperatures and Cr_2O_3 contents on the properties and microstructures of RM–Al_2O_3 composite ceramics have been investigated by adding 10% RM and different contents of Cr_2O_3 to alumina, and the optimal sintering temperatures and addition amounts have been determined. The wetting behavior of Cu on the samples at elevated temperatures have been investigated by using the seated drop method, while the surface energy of the composite ceramics at high temperature has been estimated based on the data obtained from high-temperature contact angle measurements, so as to explore the possibility of applying RM–Al_2O_3 composite ceramics in the field of electronic packaging.

2. Materials and Methods

2.1. Raw Materials

The Al_2O_3 powder (200 nm, $Al_2O_3 \geq 99.9\%$) used in this study was produced by Beasley New Materials Co. (Suzhou, China). Cr_2O_3 powder (100 nm, $Cr_2O_3 \geq 99.9\%$) was produced by Hebei Yuanying New Materials Co. (Xingtai, China). Red mud was provided by Guangxi Huayin Aluminium Co., Ltd. (Baise, China)., and Fe_3O_4 in red mud was separated by strong magnetic separation. The red mud was dried in a drying oven at 120 °C for 24 h. The dried mass was crushed using a pulverizer. The composition of the

red mud analyzed by XRF is shown in Table 1. Stearic acid, polypropylene, and paraffin were produced by Shanghai McLean Biochemical Technology Co. (Shanghai, China) Cu (≥99.95%) used was produced by CMT New Materials Co. (Attleboro, MA, USA) and processed into 3 mm × 3 mm × 3 mm cubes by wire cutting.

Table 1. The chemical composition of red mud (wt.%).

Fe_2O_3	Al_2O_3	SiO_2	CaO	Na_2O	TiO_2	Loss
29.60	18.90	16.90	15.60	11.10	5.78	2.12

2.2. Preparation of Composite Ceramics

The powder ingredients were proportioned in accordance with the composition presented in Table 2. In addition, 1 g of polypropylene, 1 g of paraffin, and 1 g of stearic acid were additionally added to the mixed powder (30 g total weight). A high-energy planetary ball mill was employed to grind the mixed powder for a duration of 30 h at a rotational speed of 300 revolutions per minute, utilizing anhydrous ethanol as the grinding medium. The mixed slurry was subjected to vacuum drying at 70 °C for 24 h in a drying oven. Subsequently, the dried mass was finely ground using an onyx mortar and then sieved through an 80-mesh sieve. The powder was pressed into 40 mm × 4 mm × 10 mm slabs using a hydraulic press at 15 MPa for 3 min. The samples were sintered using a $MoSi_2$ electric furnace (KSL-1700-2A). The temperature was ramped up to 1200 °C at a rate of 5 °C/min, followed by a further ramp-up to the target temperature at a rate of 2 °C/min. The target temperature was maintained for 2 h, and then the samples were cooled with the furnace. Additionally, each sample required a debinding process where it was held at 800 °C for 2 h.

Table 2. Chemical compositions (wt.%) of the samples.

Sample	Al_2O_3	RM	Cr_2O_3
A	100	0	0
ARC0	90	10	0
ARC1	89.1	9.9	1
ARC2	88.65	9.85	1.5
ARC3	88.2	9.8	2
ARC4	87.75	9.75	2.5
ARC5	87.3	9.7	3

2.3. Characterization of Composite Ceramics

The test samples underwent pre-treatment prior to conducting the tests. The ceramic samples were individually polished using 2.5 w and 1 w abrasive pastes, respectively. Subsequently, the ceramic samples with observed surface morphology were subjected to etching using an etching solution (3% HF, 5% HN_3) for a duration of 1 min in order to eliminate the glassy phase. The elemental composition of the red mud was analyzed using an X-ray fluorescence spectrometer (S8 TIGER, BRUKER, Berlin, Germany). Following this, ultrasonic cleaning was performed on the ceramic samples in anhydrous ethanol for a period of 5 min. X-ray diffraction analyses were carried out using an X-ray diffractometer (MiniFlex600-C, Rigaku Co., Ltd., Akishima, Japan) at 40 kV/15 mA, with a scanning range of 10~85 at a 2θ angle and a scanning speed of 5 °/min. A scanning electron microscope (SU8020, Hitachi High-Technologies, Tokyo, Japan) was used to observe the surface morphology and fracture morphology of the samples. The apparent density of the composite ceramics was measured using the Archimedes drainage method, and the densification was expressed as the ratio of the apparent density to the theoretical density. The phase compositions of the samples were analyzed semi-quantitatively by EDS (energy-dispersive X-ray spectroscopy). Vickers hardness tester was used to measure the hardness

of the samples (loading force 5 Kg, holding pressure 15 s), and in each group of 4 specimens, each specimen was tested in 10 different positions, and then the average value was taken.

The samples were machined into 40 mm × 3 mm × 6 mm blocks by diamond wire cutting, the fracture toughness of the samples was measured using the single edge notched beam (SENB) method as shown in Figure 1a, and the loading speed was 0.5 mm/min during the test. The fracture toughness K_{IC} is calculated from Equation (1):

$$K_{IC} = Y\frac{3PL}{2bh^2}\sqrt{a} \tag{1}$$

where Y is the shape factor, P is the fracture load, L is the support span, a is the depth of the cut, b is the width, w is the thickness, and c is the width of the cut. When span length/thickness/width = 8:2:1, the shape factor Y is as follows:

$$Y = 1.96 - 2.75\left(\frac{a}{h}\right) + 13.66\left(\frac{a}{h}\right)^2 - 23.98\left(\frac{a}{h}\right)^3 + 25.22\left(\frac{a}{h}\right)^4 \tag{2}$$

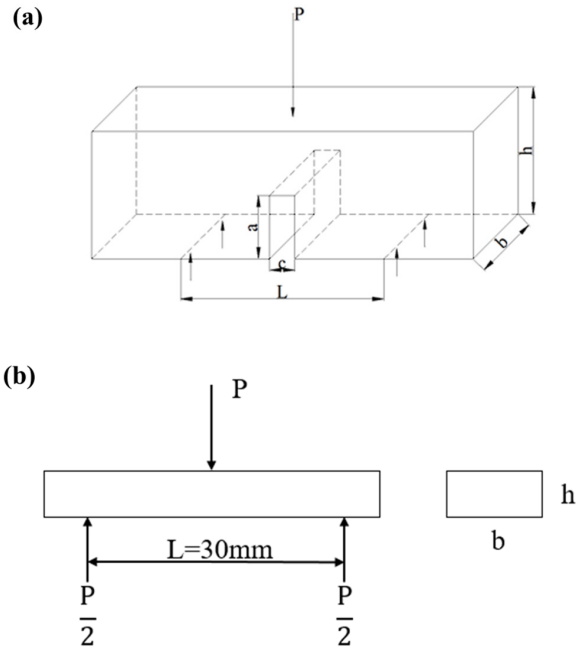


Figure 1. (**a**) Single edge notched beam schematic. (**b**) Flexural strength test schematic.

The flexural strength was measured by the three-point bending method as shown in Figure 1b. The size of the specimen was 40 mm × 3 mm × 12 mm, and the loading speed during the test was 0.5 mm/min. The bending strength can be calculated by Equation (3):

$$\sigma = \frac{3PL}{2Bh^2} \tag{3}$$

where P is the fracture load, L is the support span, b is the width, and h is the thickness.

High-temperature wettability tests were performed in a vacuum tube furnace (KJ-GSL-1800X, Hefei, China). The oxide film on the surface of the copper used for the test was polished with sandpaper and ultrasonically cleaned in anhydrous ethanol. The copper particles were placed on the ceramic samples and heated together in a vacuum tube furnace. The temperature was ramped up to the target temperature at a rate of 10 °C/min and held for ten minutes, and when the copper droplets were stabilized, a high-definition camera was used to take pictures. Finally, the contact angle was calculated using ImageJ (1.54v) software. The contact angles of Cu droplets with ceramics were measured at 1133, 1183, 1233, 1283, and 1333 °C, respectively.

3. Results and Discussion

3.1. Phase Composition

Figure 2a shows the XRD patterns of ARC2 samples sintered at different temperatures for 2 h. The main phases in the sample are corundum and $CaAl_{12}O_{19}$ (CA6), with small amounts of calcium silicate, quartz, pyroxene, and NaFe $(SiO_3)_2$. As the sintering temperature rises, most of the silicate is gradually burnt out. The XRD patterns of samples sintered at 1500 °C for 2 h, ranging from ARC1 to ARC5, are depicted in Figure 2b. The composition of the phases remains unchanged. It is worth noting that an increase in Cr_2O_3 content leads to a slight shift of the diffraction peak towards smaller angles. This can be attributed to that the formation of a complete replacement solid solution between Cr^{3+}(0.64 m) and Al^{3+} (0.57 nm), resulting in the lattice constant changing, which results in a small shift in the diffraction peak [11].

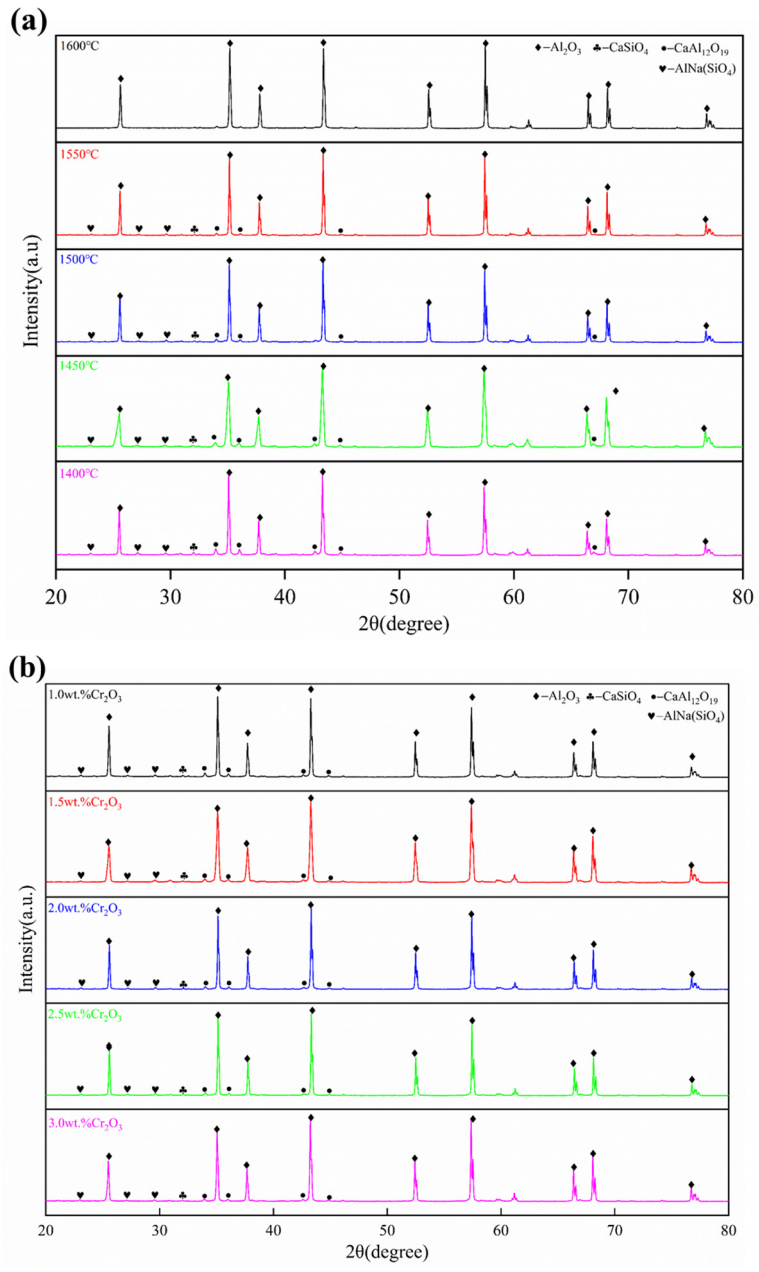


Figure 2. XRD patterns of the samples: (**a**) ARC2 samples sintered at different temperatures for 2 h; (**b**) ARC1~ARC5 samples sintered at 1500 °C.

Figure 3a shows the EDS data of the corroded ARC4 sample. Based on the compositional data of the point energy spectra, it can be judged that the columnar grains in the matrix are alumina crystals, and the hexagonal flake particles are $CaAl_{12}O_{19}$. From the surface spectral analysis, it is observed that the Ca element is concentrated in the hexagonal flake particles, and the Cr element is uniformly distributed in the matrix. Figure 3b shows the EDS data of the uncorroded AR sample. From the results of the surface spectrum analysis, Na and Si elements are mainly concentrated at the grain boundaries, and Fe elements are uniformly distributed in the matrix, with a slightly higher concentration at the grain boundaries. From the results of the point energy spectra, the silicate phase mainly shows an amorphous pattern distributed between the alumina grains and fills the grain-to-grain voids.

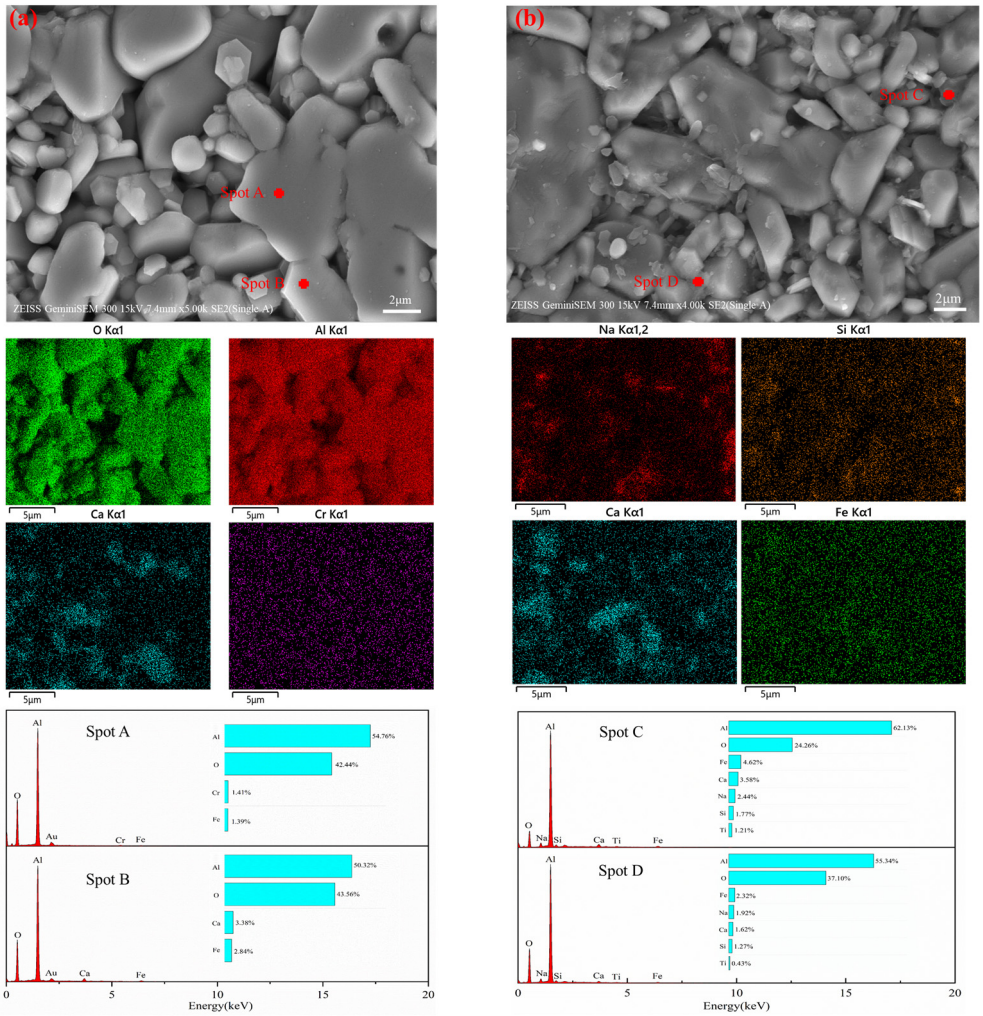


Figure 3. EDS results of composite ceramics: (**a**) ARC4 samples after 1 min in corrosion solution; (**b**) ARC0 samples not corroded by corrosion solution.

3.2. Microstructural Characterization

Figure 4b–f shows SEM images of ARC2 sintered at different temperatures for 2 h. The samples sintered at 1400 °C have been incompletely sintered, with more holes inside, and the microstructure consists of fine equiaxed grains and a few hexagonal lamellar particles. The CA6 grain exhibits preferential growth along the basal plane, and the coupled diffusion of Ca^{2+} and O^{2-} from the Ca-rich phase to the Al-rich phase controls the formation of CA6. This anisotropy of growth rate leads to the formation and growth of CA6, preferring the orientation of the base plane which is perpendicular to the reaction front, which leads flaky CA6 being obtained after reaction and sintering [12,13]. The samples sintered at

1450 °C exhibit abnormally grown grains with surface pores. This phenomenon can be attributed to the rapid decrease in the viscosity of the glassy phase, which facilitates gas diffusion in the liquid phase and subsequently leads to pore formation on the ceramic body's surface. A significant number of plate-like grains are observed in the samples sintered at 1500 °C. This phenomenon can be attributed to the formation of a small quantity of liquid phase within the lower-melting-point oxides present in the red mud. The uneven distribution of this liquid phase leads to the coexistence of dry and wet interfaces, resulting in variations in interfacial energy between the base surface of Al_2O_3 grains and other interfaces. Consequently, different growth rates occur on different surfaces, leading to anisotropic growth in certain grains [14].

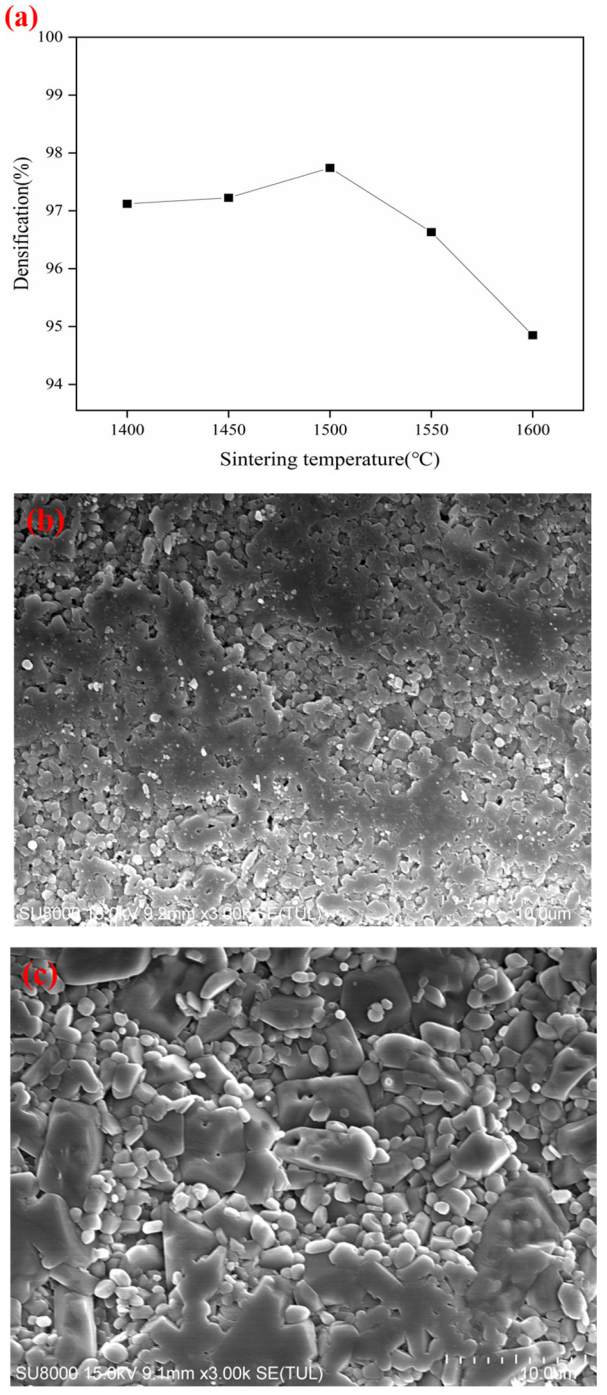


Figure 4. *Cont.*

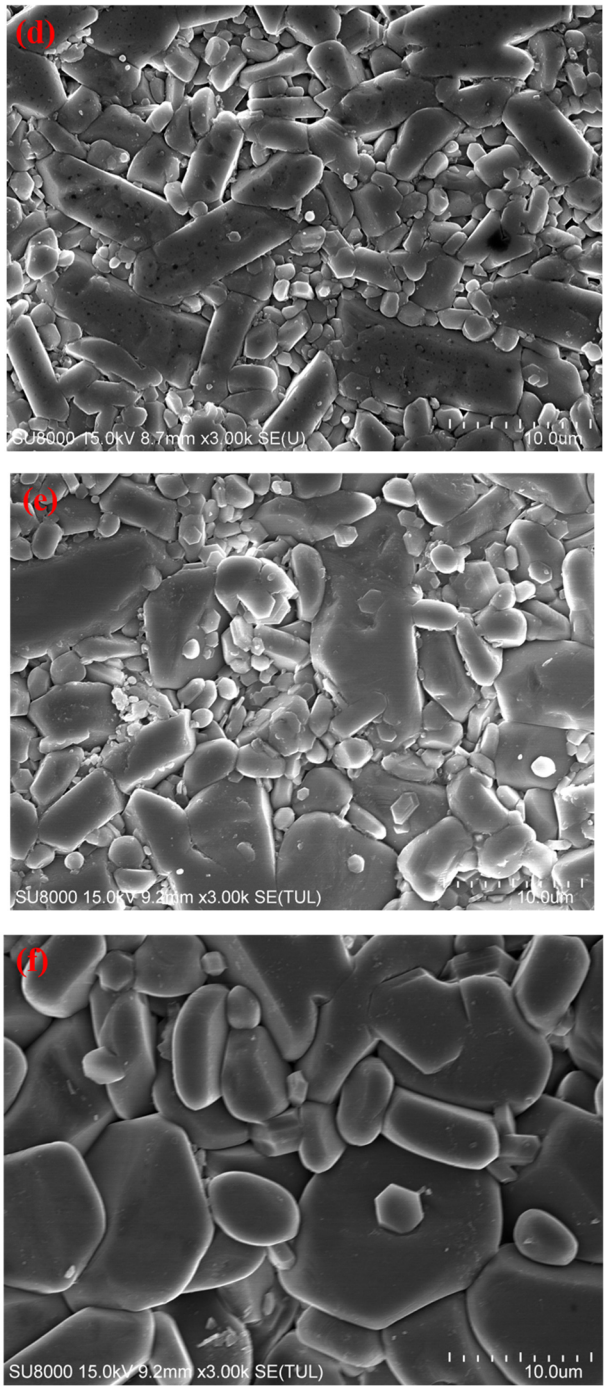


Figure 4. SEM micrographs of ARC2 sintered at different temperatures for 2 h: (**a**) densification of ARC2; (**b**) 1400 °C; (**c**) 1450 °C; (**d**) 1500 °C; (**e**) 1550 °C; (**f**) 1600 °C.

The densifications profiles of ARC2 samples sintered at various temperatures for 2 h are depicted in Figure 4a. It can be observed that the densifications of the composite ceramic exhibit a gradual increase followed by a rapid decrease with increasing temperature. In the initial stage of ceramic sintering, the bonding between the particles is weak, and there are more pores in the material. As the temperature increases, sintering and solid-state diffusion begin to occur between the particles, the pores are gradually filled, the material becomes denser, and the density gradually increases. The maximum densification achieved is 97.75% for samples sintered at 1500 °C. Obvious lath-like grains can be observed from Figure 4d. This is in agreement with the findings of Cahoon et al. [15]. They observed

relatively uniform-sized anisotropic growth grains in pure alumina ceramics, which appeared abruptly as the matrix approached final densification. The densities of the composite ceramics decreased rapidly when the sintering temperature exceeded 1500 °C. The density of the composite ceramics sintered at 1600 °C for 2 h was 94.85%. According to the classical equation for grain growth kinetics:

$$G^n - G_0^n = K \cdot t \tag{4}$$

where G is the grain size, G_0 is the initial grain size, n is the growth index, K is a temperature-dependent constant, and t is the sintering time. This equation shows that the grain size increases with time and temperature. According to the Arrhenius equation, the grain growth rate constant K is related to the temperature T as follows:

$$K = K_0 \exp\left(\frac{-Q}{RT}\right) \tag{5}$$

where K_0 is a constant, Q is the activation energy for grain boundary migration, R is the gas constant, and T is the absolute temperature. At high temperatures, the K value increases significantly, and the grain growth rate is accelerated, especially in the late stage of high-temperature sintering, and the abnormal grain growth phenomenon is more obvious. Samples sintered at 1600 °C have very coarse grains, as shown in Figure 4f. In the case of abnormal grain growth, the larger grains occupy more volume, while the smaller grains are more difficult to move and cannot completely eliminate the inter-grain porosity. Especially, larger residual pores may form between large grains. During normal grain growth, the grain boundaries migrate uniformly and can effectively reduce the pores. However, at the interface between abnormally grown grains and small grains, the grain boundaries migrate unevenly, making it difficult to fill the pores in these regions. As a result, the densification of the material decreases and the porosity increases.

Figure 5b–f shows the surface morphology of ARC1~ARC5. Overall, the effect of Cr_2O_3 content on crystal morphology is not obvious. When the Cr_2O_3 content increased to 2.5 wt.%, obvious holes were observed in the matrix.

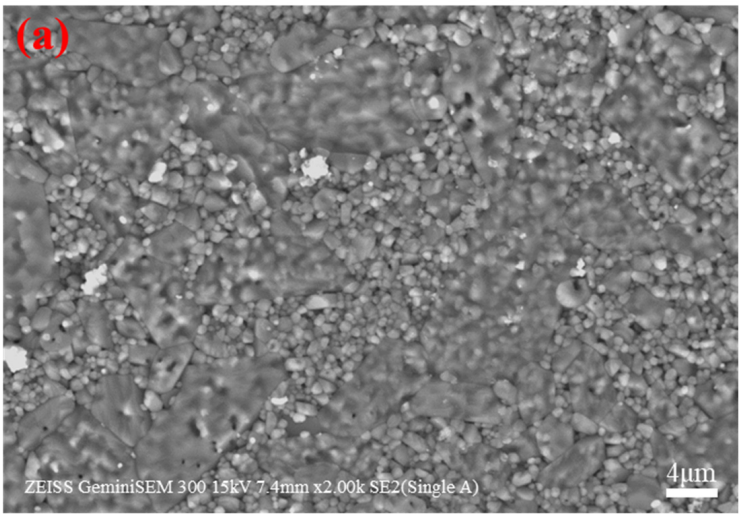


Figure 5. *Cont.*

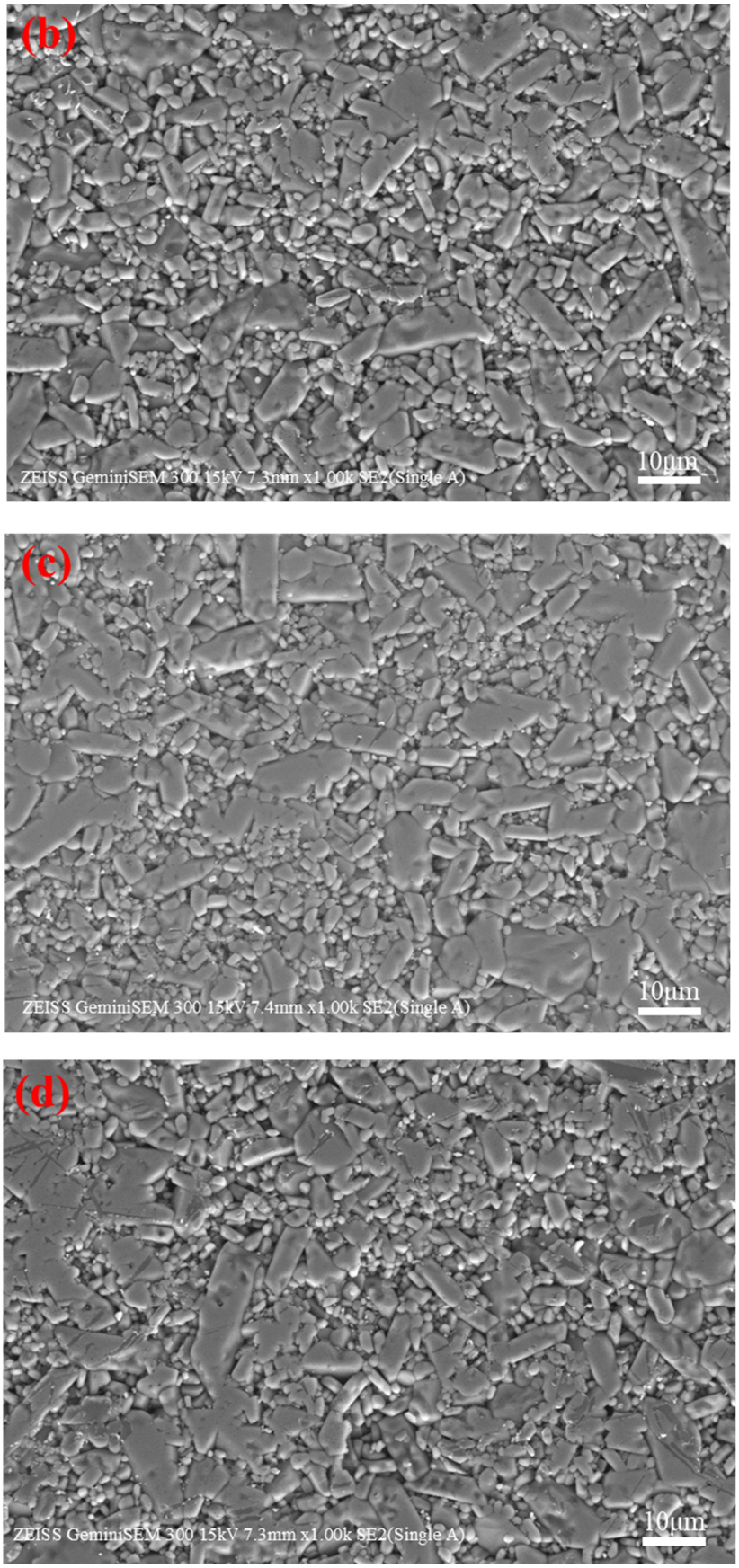


Figure 5. *Cont*.

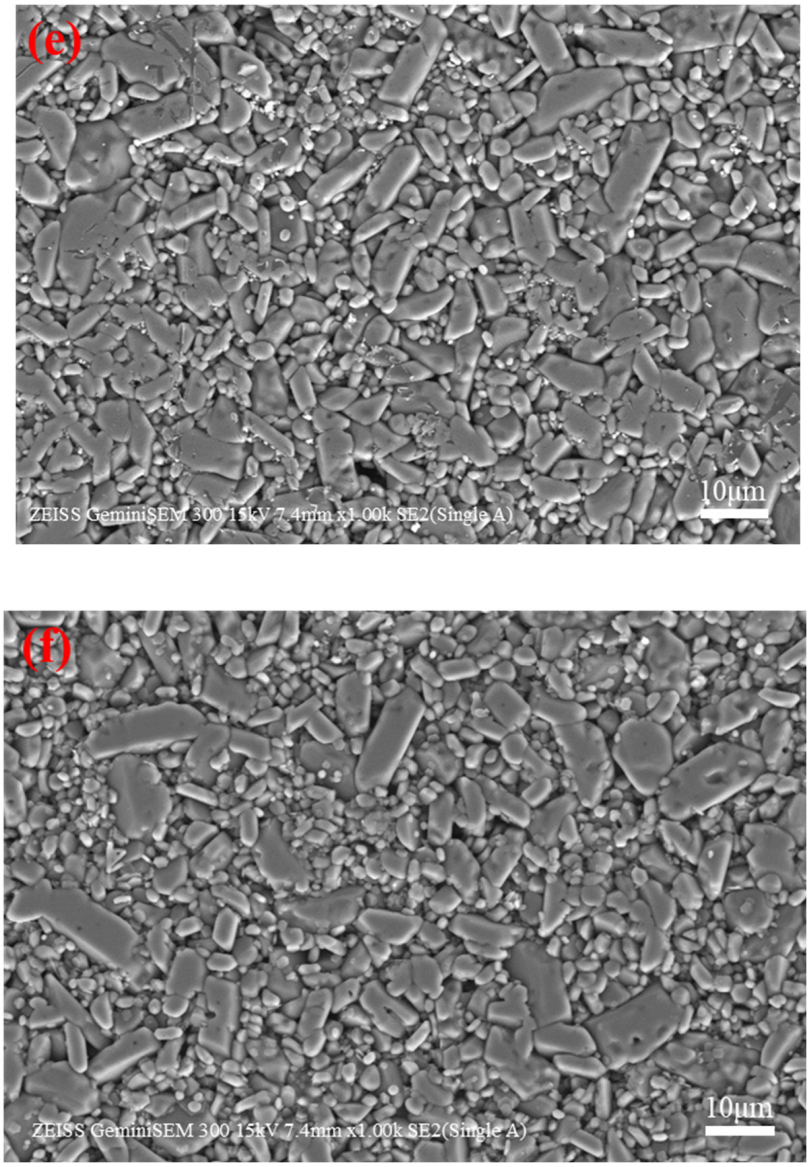


Figure 5. SEM micrographs of different samples sintered at 1500 °C: (**a**) A; (**b**) ARC1; (**c**) ARC2; (**d**) ARC3; (**e**) ARC4; (**f**) ARC5.

The densification of pure alumina specimens sintered at 1500 °C for 2 h was 92.14%. Figure 5a shows an incompletely densified structure with uneven grain size distribution and a large number of holes in the matrix. In the case of alumina, ordinary sintering at atmospheric pressure is usually above 1650 °C. The addition of red mud makes a small amount of liquid phase appear in the matrix, which accelerates the mass transfer rate during the sintering process. At the same time, under the action of capillary force generated by the liquid phase, it causes pressure and sliding between particles, which prompts the original particles to rearrange and improves the particle packing density. Based on this, this study determined that the optimum sintering temperature of ARC composite ceramics is 1500 °C, while the addition of red mud can effectively reduce the sintering temperature of Al_2O_3 ceramics.

3.3. Mechanical Properties

Figure 6a,b show the flexural strength and hardness of ARC2 sintered at different temperatures for 2 h. With the increase in sintering temperature, the flexural strength and Vickers hardness of the samples increase first and then decrease. The maximum

flexural strength of the sample sintered at 1500 °C is 297.03 MPa, and the hardness value is 17.44 GPa. This is because, when sintered below 1500 °C, the sample presents an incomplete sintering state, retains more original particles, has poor interfacial binding force, and has more pores, which is mainly inter-granular fracture. When the sintering temperature is higher than 1500 °C, the grains in the matrix grow rapidly, and along with the liquid phase volatilization at a low boiling point in the grain boundary, the density of the sample decreases, resulting in a decrease in strength. The flexural strength of the sample sintered at 1600 °C is higher than that of the sample sintered at 1550 °C, because as the grain grows, it is more difficult for the crack to bypass the large grain in the process of expansion, resulting in a significantly higher proportion of trans-granular fracture (as shown in Figure 7a).

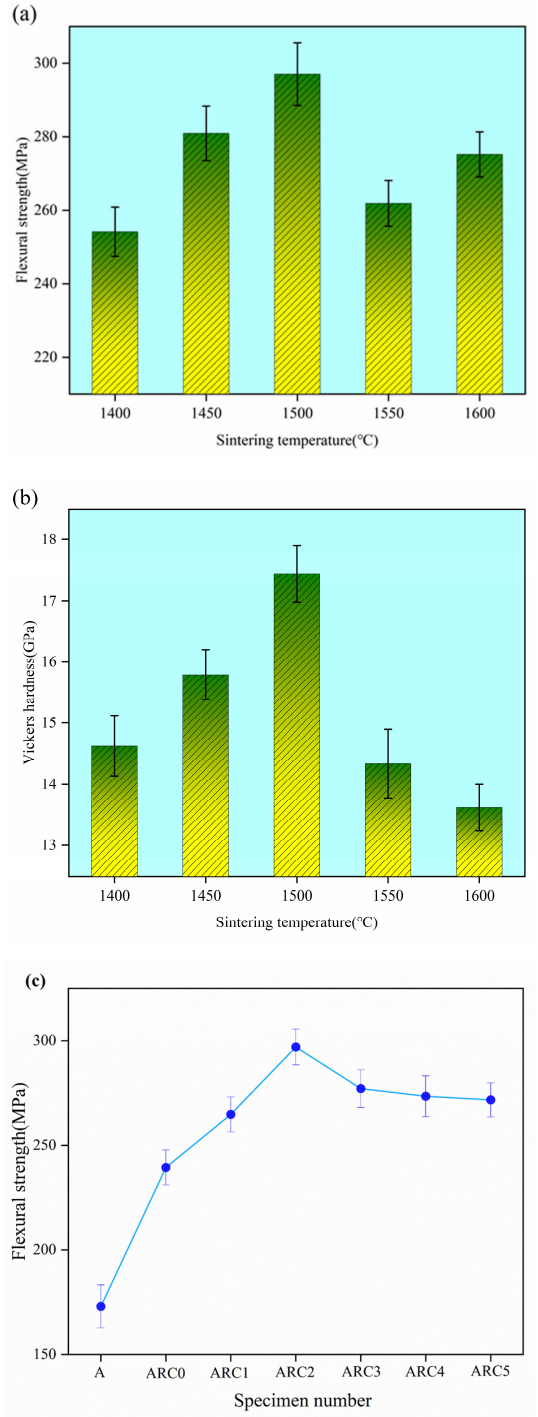


Figure 6. *Cont.*

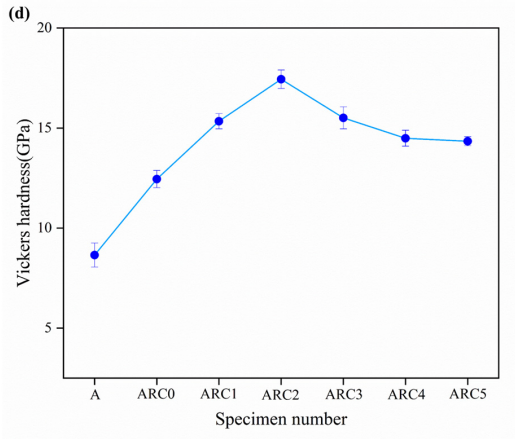


Figure 6. Mechanical properties of samples: (**a**) flexural strength of ARC2 sintered at different temperatures; (**b**) Vickers hardness of ARC2 sintered at different temperatures; (**c**) flexural strength of A~ARC5; (**d**) Vickers hardness of A~ARC5.

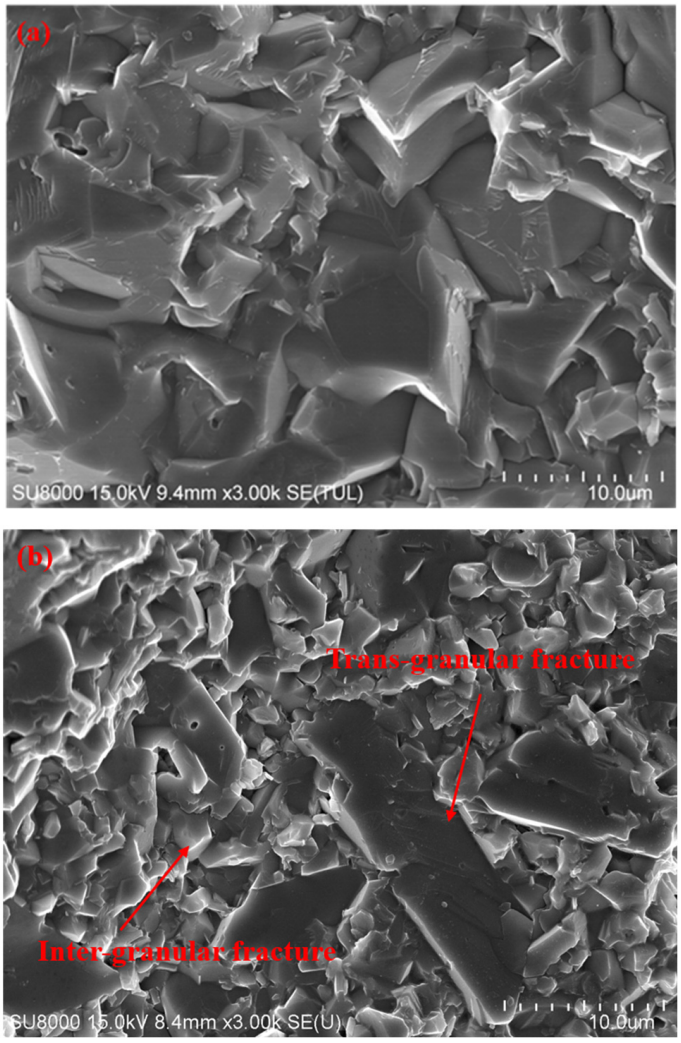


Figure 7. *Cont.*

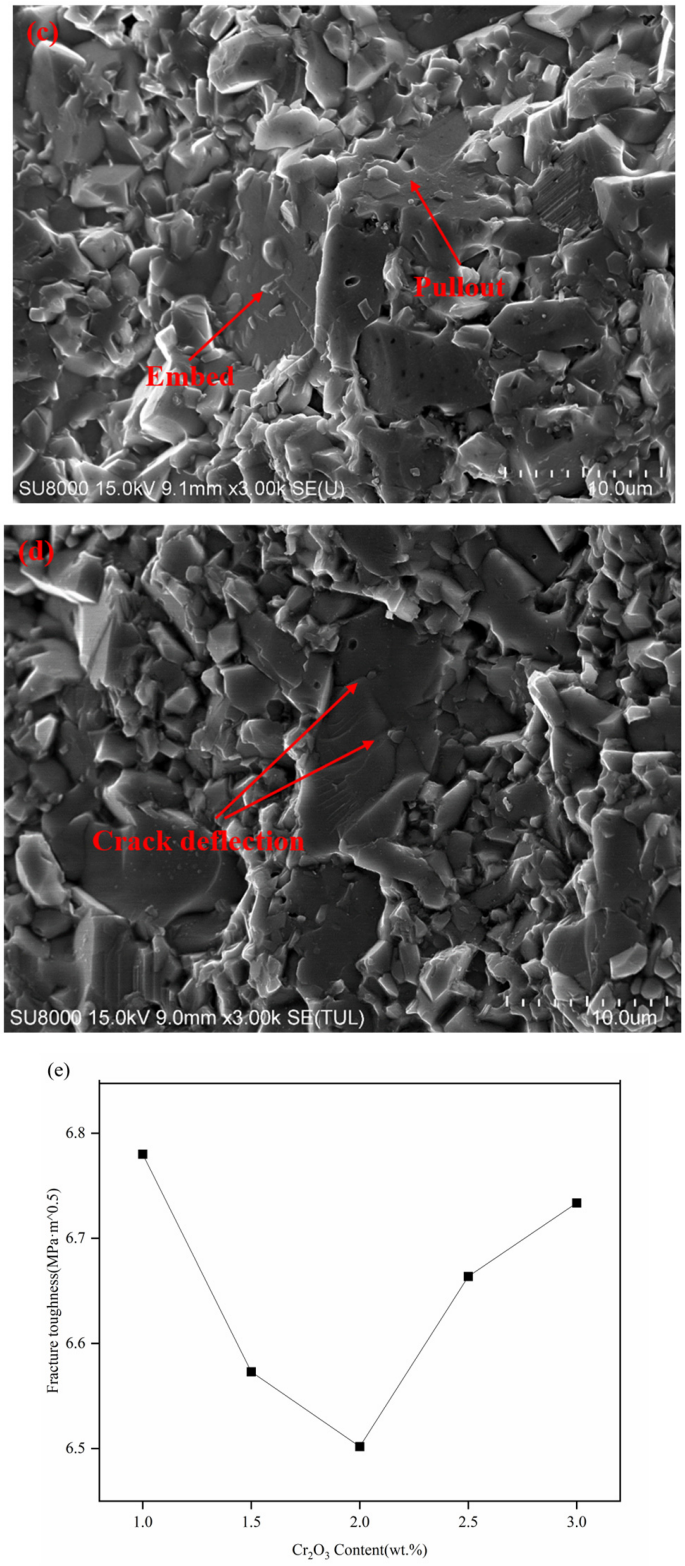


Figure 7. Fracture morphologies of some samples: (**a**) ARC2 sintered at 1600 °C; (**b**) ARC1 sintered at 1500 °C; (**c**) ARC4 sintered at 1500 C; (**d**) ARC2 sintered at 1500 °C; (**e**) toughness of ARC1~ARC5 sintered at 1500 °C.

Figure 6c,d show the flexural strength and hardness of A~ARC5 sintered at 1500 °C. Since the pure alumina specimen was not fully sintered, its flexural strength was only 173.5 MPa, and its hardness was 8.65 GPa. Notably, the sample containing 1.5 wt.% Cr_2O_3

exhibits the highest flexural strength. In the early stage of sintering, Cr^{3+} is easily enriched on the surface of Al_2O_3 grains [16,17]. Due to the solid solution of Cr ions, the distortion energy of the Al_2O_3 grain interface is increased, and the growth rate of the chromium-rich interface is accelerated, which promotes the sintering of ceramic samples. On the other hand, the increase in grain-boundary distortion energy has a positive effect on hindering the dislocation motion, thus enhancing the flexural strength of the composite ceramics. The mechanical properties of ceramics are very sensitive to defects such as porosity and cracks. Cr_2O_3 is unstable under atmospheric pressure sintering and is easily converted to CrO_3 through a gasification–condensation mechanism, leading to a decrease in the densification of the ceramic samples. Consequently, the flexural strength and hardness of the ceramic samples increase and then decrease with the increase in Cr_2O_3 content.

The fracture morphologies of some samples are depicted in Figure 7, exhibiting a combination of through-crystal and inter-granular fractures. The growth of CA6 exhibits a strong preferred crystallographic orientation, and the reaction primarily occurs by the diffusion of Ca^{2+} into Al_2O_3. The distribution of CA6 phase in the matrix can be observed in three different forms. Firstly, they distribute at the grain boundaries and fill the voids between grains, which enhances material densification and reduces porosity and pore size, thereby improving the strength of the composite material [18]. Secondly, CA6 grows along the surface of Al_2O_3 grains, which prolong the path of crack growth and increase the energy required for crack growth during inter-granular fracture and thus improve the fracture toughness of the material [19]. However, due to the introduction of less Ca element, CA6 growing in the Al_2O_3 grain is very thin, so it can provide a limited strengthening effect, as shown in Figure 7c.

It is worth noting that in the third case, CA6 is embedded between the Al_2O_3 grains at different angles and forms an "endo-crystalline" structure with the Al_2O_3 grains [20,21], as shown in Figure 7c. CA6 and Al_2O_3 have similar coefficients of thermal expansion (8.0×10^{-6} °C^{-1}, 8.6×10^{-6} °C^{-1}, respectively) [22], and it is generally believed that CA6 and Al_2O_3 do not undergo thermal mismatch and have good compatibility in the matrix. However, this is limited to the independent existence of CA6 grains and Al_2O_3 grains, because there are gaps between grains to make up for this difference. And from the perspective of the crystal structure of CA6 and Al_2O_3, the thermal expansion behavior of the two phases is anisotropic, and the occurrence of thermal mismatch is predictable when CA6 grows at different angles within the Al_2O_3 grains. This kind of structure will produce micro-cracks at the sub-interface, weaken the effect of the main grain boundary, inhibit the dislocation movement during the fracture process, play the role of crack pinning and change the expansion direction of the main crack, and may change its fracture mode, i.e., from the original inter-granular fracture to trans-granular fracture, as shown in Figure 7d.

3.4. Wettability at High Temperature

Al_2O_3 ceramics have been extensively utilized in the fabrication of ceramic substrates and ceramic cleavers [23]. With increasing demand for lower costs in semiconductor packaging, the adoption of low-cost bonding wire becomes imperative. Consequently, copper wire will inevitably replace gold wire as the primary alternative for bonding wire in the future. By investigating the wetting behavior and interface reactions of Cu liquid on RM–Al_2O_3 composite ceramic materials at elevated temperatures, this research establishes a fundamental framework for the potential application of RM–Al_2O_3 composite ceramic materials in the field of electronic packaging.

The contact angle data of Cu and RM–Al_2O_3 composite ceramics at different temperatures are presented in Figure 8. It can be observed that the contact angle gradually decreases with increasing temperature. Moreover, all contact angles measured at temperatures above the melting point are greater than 90°, indicating the non-wetting behavior of Cu and ARC composite ceramic. The SEM images in Figure 9 illustrate the wetted interface of ARC2 with Cu droplets, revealing a clean and flat interface without any dissolution or presence of reactants. It shows that at high temperature, the elements of red mud such as iron,

nickel, sodium, calcium, and silicon in RM–Al_2O_3 composite ceramics have no diffusion phenomenon, and there is no pollution of copper liquid.

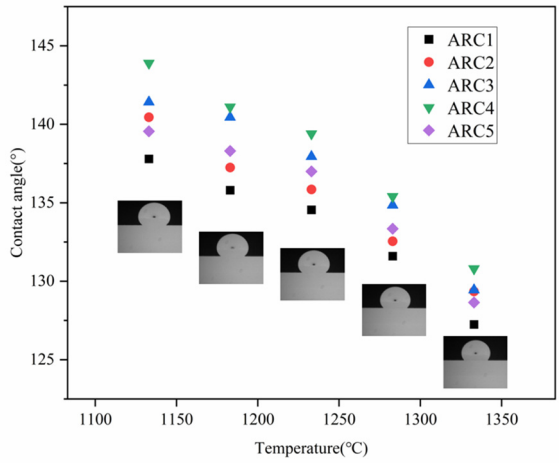


Figure 8. Contact angle of samples' surfaces with Cu.

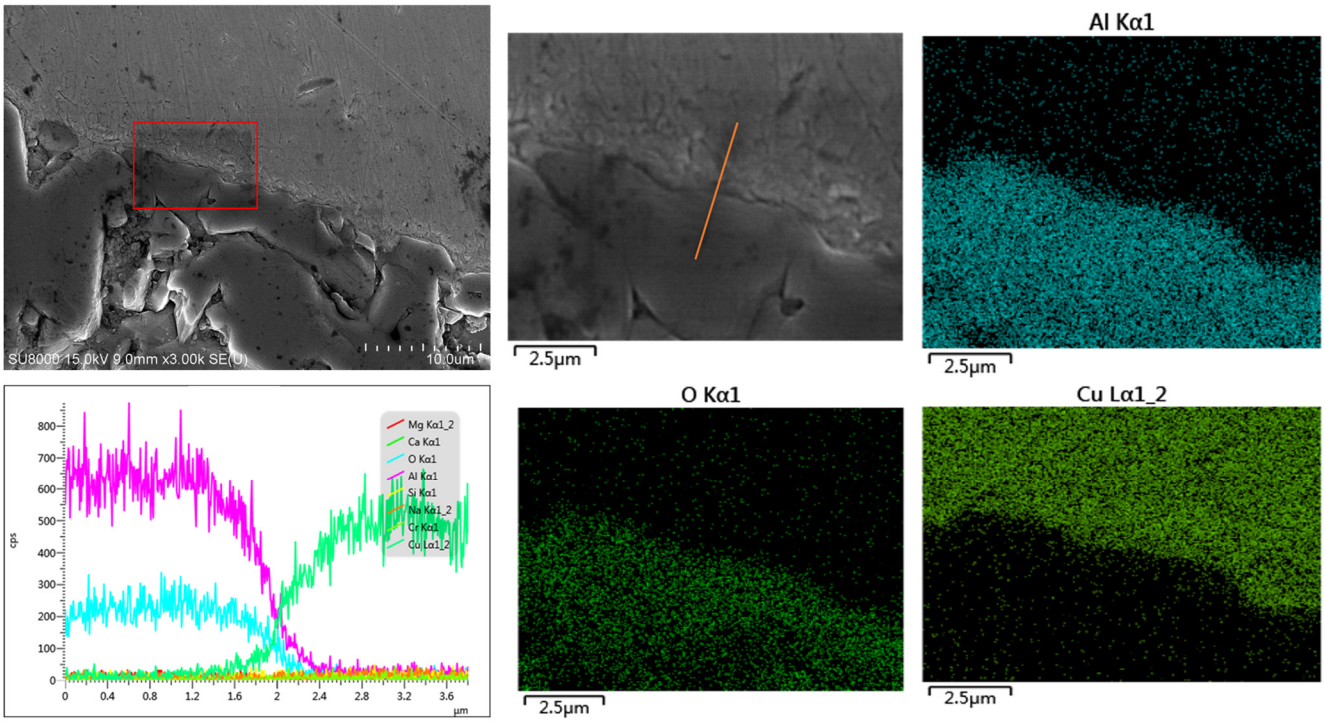


Figure 9. SEM and EDS images of ARC2–Cu interface. The red square are face-scanning area and the lines are line-scanning area.

Thomas Young proposed the contact angle of a liquid as the mechanical equilibrium of the drop resting on a plane solid surface at the three-phase boundary.

$$\gamma_{lv}\cos\theta = \gamma_{sv} - \gamma_{sl} \tag{6}$$

The London dispersion theory is employed by Berthelot [24] to calculate interfacial tension based on the surface tensions of two phases, using the geometric mean combination rule:

$$\gamma_{sl} = \gamma_s + \gamma_l - 2\sqrt{\gamma_s\gamma_l} \tag{7}$$

The surface tension of Cu can be calculated from the following equation [25]:

$$\gamma_l = 1.32 - 2.8 \times 10^{-4}(T - 1358) \quad (8)$$

The experimental values obtained by measuring the contact angle of copper and ceramics at different temperatures are plotted as cosθ vs. γ_l. The Zismen approximation was employed to establish a linear correlation between cosθ and γ_l:

$$\cos\theta = a\gamma_l + b \quad (9)$$

The above equations are ultimately interconnected to establish the correlation between γ_s and T:

$$\gamma_s = AT^3 + BT^2 + CT + D \quad (10)$$

The fitted parameters are presented in Table 3. The surface energy data from ARC1~ARC5 have been compared with the surface energy results for aluminum oxide reported by Eustathopoulos et al. [26] (γ_s = 20.77 − 0.007083 T), as illustrated in Figure 10. The surface energy of ARC composite ceramics decreases more slowly as the temperature decreases than that of Al_2O_3, and ARC3 and ARC4 have higher surface energy than Al_2O_3 at high temperature. As the Cr content increases, the wettability of Cu on the composite ceramic becomes worse. This can be explained in two ways. With the increase in Cr oxide, the solid solution of Cr ions in Al_2O_3 increases, leading to an increase in lattice distortion, which leads to an increase in the surface energy of the composite ceramics. Secondly, the excess addition of Cr led to an increase in the internal pores of the composite ceramics, which also led to an increase in the surface roughness of the material. According to the Wenzel model, on a hydrophobic surface, the larger the roughness is, the more hydrophobic it is.

Table 3. Values of fitting parameters and corresponding calculation.

Sample	a	b	R^2	A	B	C	D
ARC1	−2.32	2.28	0.94	-2.95×10^{-11}	1.82×10^{-8}	−0.0027	13.90
ARC2	−2.37	2.34	0.98	-3.08×10^{-11}	2.00×10^{-8}	−0.0028	14.43
ARC3	−2.56	2.55	0.92	-3.60×10^{-11}	2.91×10^{-8}	−0.0032	16.34
ARC4	−2.68	2.69	0.96	-3.94×10^{-11}	3.47×10^{-8}	−0.0035	17.68
ARC5	−2.38	2.33	0.92	-3.11×10^{-11}	2.24×10^{-8}	−0.0028	14.36

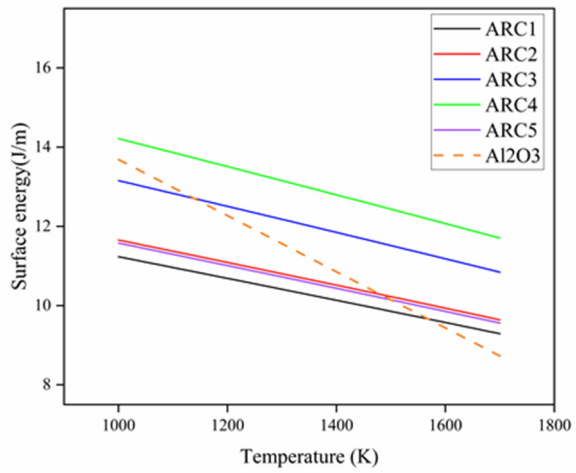


Figure 10. Surface energy of ARC1~ARC2 at high temperature.

4. Conclusions

Using red mud, Al_2O_3, and Cr_2O_3 as raw materials, high-performance red mud alumina composite ceramics have been prepared by press-free sintering. The experimental results demonstrate the following:

(1) Red mud can significantly lower the sintering temperature of Al_2O_3 ceramics. The samples sintered at 1500 °C with the addition of 1.5 wt.% Cr_2O_3 have better properties, with a bending strength of 297.03 MPa, a fracture toughness of 6.50 MPa/$m^{1/2}$, a hardness value of 17.44 GPa and a densification of 97.75%.

(2) There are three different distributions of CA6 in ARC composite ceramics. CA6 distributing at grain boundaries can fill the voids between grains and improve the densification of the ceramics. CA6 distributing parallel to the Al_2O_3 grains extends the crack propagation path. CA6 and alumina grains form an "endo-crystalline" structure, which can change the direction of crack propagation and transform from an inter-granular fracture to trans-granular fracture.

(3) Cu liquid does not wet the ARC composite ceramics at high temperatures, no chemical reaction occurs at the interface, and there is no elemental diffusion into Cu liquid. Moreover, the ARC composite ceramics have a higher surface energy than Al_2O_3 at high temperatures and decrease more slowly with temperature.

Author Contributions: Conceptualization, S.J. and A.L.; methodology, S.J.; investigation, S.J.; formal analysis, S.J.; writing—original draft, S.J. and Z.W.; funding acquisition, A.L.; resources, A.L.; supervision, A.L.; writing—review and editing, A.L.; data curation, Z.W. All authors have read and agreed to the published version of the manuscript.

Funding: This research was funded by the Specific Research Project of Guangxi for Research Bases and Talents, grant number GuiKeAD21238010. 2021 Special funds for central guidance of local scientific and technological development funds, grant number GuiKeZY21195030. Guangxi Key Research and Development Program, grant number GuiKeAB22080015.

Data Availability Statement: Data are contained within the article.

Conflicts of Interest: The authors declare no conflicts of interest.

References

1. Liu, R.-X.; Poon, C.-S. Utilization of red mud derived from bauxite in self-compacting concrete. *J. Clean. Prod.* **2016**, *112*, 384–391. [CrossRef]
2. Zhang, N.; Li, H.; Liu, X. Hydration mechanism and leaching behavior of bauxite-calcination-method red mud-coal gangue based cementitious materials. *J. Hazard. Mater.* **2016**, *314*, 172–180. [CrossRef] [PubMed]
3. Wang, W.; Chen, W.; Liu, H.; Han, C. Recycling of waste red mud for production of ceramic floor tile with high strength and lightweight. *J. Alloys Compd.* **2018**, *748*, 876–881. [CrossRef]
4. He, H.; Yue, Q.; Qi, Y.; Gao, B.; Zhao, Y.; Yu, H.; Li, J.; Li, Q.; Wang, Y. The effect of incorporation of red mud on the properties of clay ceramic bodies. *Appl. Clay Sci.* **2012**, *70*, 67–73. [CrossRef]
5. Pérez-Villarejo, L.; Corpas-Iglesias, F.A.; Martínez-Martínez, S.; Artiaga, R.; Pascual-Cosp, J. Manufacturing new ceramic materials from clay and red mud derived from the aluminium industry. *Constr. Build. Mater.* **2012**, *35*, 656–665. [CrossRef]
6. Gonzalez Triviño, I.; Pascual-Cosp, J.; Moreno, B.; Benítez-Guerrero, M. Manufacture of ceramics with high mechanical properties from red mud and granite waste. *Mater. Construcción* **2019**, *69*, 180. [CrossRef]
7. Nath, M.; Kumar, P.; Maldhure, A.V.; Sinhamahapatra, S.; Dana, K.; Ghosh, A.; Tripathi, H.S. Anomalous densification behavior of Al_2O_3–Cr_2O_3 system. *Mater. Charact.* **2016**, *111*, 8–13. [CrossRef]
8. Kafkaslıoğlu Yıldız, B.; Yılmaz, H.; Tür, Y.K. Evaluation of mechanical properties of Al_2O_3–Cr_2O_3 ceramic system prepared in different Cr_2O_3 ratios for ceramic armour components. *Ceram. Int.* **2019**, *45*, 20575–20582. [CrossRef]
9. Azhar, A.Z.A.; Choong, L.C.; Mohamed, H.; Ratnam, M.M.; Ahmad, Z.A. Effects of Cr_2O_3 addition on the mechanical properties, microstructure and wear performance of zirconia-toughened-alumina (ZTA) cutting inserts. *J. Alloys Compd.* **2012**, *513*, 91–96. [CrossRef]
10. Manshor, H.; Azhar, A.Z.A.; Rashid, R.A.; Sulaiman, S.; Abdullah, E.C.; Ahmad, Z.A. Effects of Cr_2O_3 addition on the phase, mechanical properties, and microstructure of zirconia-toughened alumina added with TiO_2 (ZTA–TiO_2) ceramic composite. *Int. J. Refract. Met. Hard Mater.* **2016**, *61*, 40–45. [CrossRef]
11. Zhao, P.; Zhao, H.; Yu, J.; Zhang, H.; Gao, H.; Chen, Q. Crystal structure and properties of Al_2O_3–Cr_2O_3 solid solutions with different Cr_2O_3 contents. *Ceram. Int.* **2018**, *44*, 1356–1361. [CrossRef]

12. An, L.; Chan, H.M.; Soni, K.K. Control of calcium hexaluminate grain morphology in in-situ toughened ceramic composites. *J. Mater. Sci.* **1996**, *31*, 3223–3229. [CrossRef]
13. Domínguez, C.; Chevalier, J.; Torrecillas, R.; Fantozzi, G. Microstructure development in calcium hexaluminate. *J. Eur. Ceram. Soc.* **2001**, *21*, 381–387. [CrossRef]
14. Song, H.; Coble, R.L. Origin and Growth Kinetics of Platelike Abnormal Grains in Liquid-Phase-Sintered Alumina. *J. Am. Ceram. Soc.* **1990**, *73*, 2077–2085. [CrossRef]
15. Cahoon, H.P.; Christensen, C.J. Sintering and Grain Growth of Alpha-Alumina. *J. Am. Ceram. Soc.* **1956**, *39*, 337–344. [CrossRef]
16. Cho, S.-A.; Arenas, F.J.; Ochoa, J. Densification and hardness of Al_2O_3–Cr_2O_3 system with and without Ti addition. *Ceram. Int.* **1990**, *16*, 301–309. [CrossRef]
17. Paek, Y.K.; Lee, H.Y.; Kang, S.J.L. Direction of Liquid Film Migration Induced by Chromic Oxide in Alumina-Anorthite. *J. Am. Ceram. Soc.* **1996**, *79*, 3029–3032. [CrossRef]
18. Kunkun, C.; Tao, F.; Yingyi, Z.; Jie, W.; Haobo, M.; Tianbiao, T. Microstructure and mechanical properties of $CaAl_{12}O_{19}$ reinforced Al_2O_3–Cr_2O_3 composites. *J. Eur. Ceram. Soc.* **2021**, *41*, 7935–7945. [CrossRef]
19. An, L.; Chan, H.M. R-Curve Behavior of In-Situ-Toughened Al_2O_3:$CaAl_{12}O_{19}$ Ceramic Composites. *J. Am. Ceram. Soc.* **1996**, *79*, 3142–3148. [CrossRef]
20. Yin, Z.; Huang, C.; Zou, B.; Liu, H.; Zhu, H.; Wang, J. Study of the mechanical properties, strengthening and toughening mechanisms of Al_2O_3/TiC micro-nano-composite ceramic tool material. *Mater. Sci. Eng. A* **2013**, *577*, 9–15. [CrossRef]
21. Bai, X.; Huang, C.; Wang, J.; Zou, B.; Liu, H. Fabrication and characterization of Si3N4 reinforced Al_2O_3-based ceramic tool materials. *Ceram. Int.* **2015**, *41*, 12798–12804. [CrossRef]
22. Xi, Z.; Jinsheng, L.; Junguo, L.; Yanan, Z.; Suju, H.; Pengyao, L.; Hao, N. The properties characterization and strengthening-toughening mechanism of Al_2O_3-CA6-MA-Ni multi-phase composites prepared by adding calcined dolomite. *Mater. Charact.* **2022**, *186*, 111810. [CrossRef]
23. Kim, I.J.; Kim, H.S.; Seo, M.Y.; Gauckler, L.J. Advanced ceramics in wire bonding capillaries for semiconductor package technology. *Mater. Sci. Eng. A* **2008**, *498*, 129–134. [CrossRef]
24. Sharma, P.K.; Rao, K.H. Analysis of different approaches for evaluation of surface energy of microbial cells by contact angle goniometry. *Adv. Colloid Interface Sci.* **2002**, *98*, 341–463. [CrossRef] [PubMed]
25. Chawla, K.K.; Withers, P.J. International Materials Reviews in 2013. *Int. Mater. Rev.* **2013**, *58*, 1. [CrossRef]
26. Bao, S.; Tang, K.; Kvithyld, A.; Engh, T.; Tangstad, M. Wetting of pure aluminium on graphite, SiC and Al_2O_3 in aluminium filtration. *Trans. Nonferrous Met. Soc. China* **2012**, *22*, 1930–1938. [CrossRef]

Disclaimer/Publisher's Note: The statements, opinions and data contained in all publications are solely those of the individual author(s) and contributor(s) and not of MDPI and/or the editor(s). MDPI and/or the editor(s) disclaim responsibility for any injury to people or property resulting from any ideas, methods, instructions or products referred to in the content.